**Noname manuscript No.**
(will be inserted by the editor)

# Quantitative structural analysis of simulated granular packings of non-spherical particles

**Ole Stenzel · Martin Salzer · Volker Schmidt · Paul W. Cleary · Gary W. Delaney**

Received: date / Accepted: date

**Abstract** A set of computationally generated granular packings of frictionless grains is statistically analyzed using tools from stochastic geometry. We consider both the graph of the solid phase (formed using the particle midpoints) and the pore-phase. Structural characteristics rooted in the analysis of random point processes are seen to yield valuable insights into the underlying structure of granular systems. The graph of the solid phase is analyzed using traditional measures such as edge length and coordination number, as well as more instructive measures of the overall transport properties such as geometric tortuosity, where significant differences are observed in the windedness of paths through the different particle graphs considered. In contrast, the distributions of pore-phase characteristics have a similar shape for all considered granular packings. Interestingly, it is found that prolate and oblate ellipsoid packings show a striking similarity between their solid-phase graphs as well as between their pore-phase graphs.

## 1 Introduction

Granular systems, such as sand, soils and powders are present throughout the natural world [22, 23], however there is still much that we do not understand about their varied and complex behaviors. Even in their static state, we have yet to develop methods sophisticated enough to fully characterize a granular

Ole Stenzel · Martin Salzer · Volker Schmidt
Institute of Stochastics, Ulm University, Germany
E-mail: ole.stenzel@uni-ulm.de
E-mail: martin.salzer@uni-ulm.de
E-mail: volker.schmidt@uni-ulm.de

Paul W. Cleary · Gary W. Delaney
CSIRO Computational Informatics, Clayton South, VIC 3169, Australia
E-mail: paul.cleary@csiro.au
E-mail: gary.delaney@csiro.au

system, and to exactly relate the physical properties of the individual grains, and their geometric configuration, to the macroscopic properties of the system.

The study of particle packings is extremely important for understanding the properties of granular materials but also has had significant impact in understanding liquids and jamming, and transitions in glasses and other materials [40,39]. Since the early experimental work of Bernal on mono-disperse sphere packings [2], systems composed of purely spherical grains have been by far the most studied. Even for the simplest mono-disperse sphere packings, a rich and varied set of behaviors are observed as the density of the packing is varied, with a key transition being found at the random close packing limit, where the system jams in its most dense disordered state. For spheres, this limit is well established at a packing fraction of $\Phi \simeq 0.64$ [2].

More recently, much attention has focused on investigating the properties of packings of non-spherical grains, which more realistically represent the multitude of grain shapes found in nature [12]. Studies of the role of anisotropy in the grain shape using spherocylinders and ellipsoids have demonstrated that the packing density in random packings varies strongly with the aspect ratio of the grains [12,8,10,29]. Baram investigated the importance of polydispersity in ellipsoid packings and showed how the contact forces between particles varied as the shape deviated away from a sphere [38]. Packings of polyhedral shapes have been shown to have a strong propensity to self-assemble into various ordered structures [37], while packings of tetrahedra have recently been the subject of considerable investigation and been shown to form hyperstatic packings [36]. The importance of particle shape has also been demonstrated in determining the physical properties of granular packings for a range of 3D printed non-spherical shapes [35], with the stress response being found to be strongly affected by the shape of the individual grains.

In this paper, we consider a set of computationally generated granular packings and perform an extensive series of analyses to quantify the geometric properties of both the solid and the pore-phase. The granular packings considered have been chosen to capture several key features seen in granular systems, and cover a range of density, anisotropy and order. The first granular system is a random close packing of spheres, which represents probably one of the most important and most studied of all granular systems [2,9,13, 38]. We then consider two different ellipsoid packings composed of prolate and oblate grains, respectively. Ellipsoids are an important grain shape that closely approximates the shape of many real grains e.g. stones, tablets, rice, etc. These packings allow us to study the effect of anisotropy of the grain shape in random granular packings [8,10,29]. Finally, we consider a packing of superballs (equiaxed superellipsoids) which have a shape similar to a rounded cube. This packing exhibits a large degree of structural ordering, and allows us to compare and contrast the effect of such ordering compared to the other less ordered packings.

A considerable part of the analysis is performed by the use of spatial graphs, which are widely applied to analyze or simulate complex structures in biology, materials science and many other areas, see e.g. [1,25,30,32]. Moreover, spatial

**Table 1** Parameters of superellipsoids together with packing fraction $\Phi$

| | $m$ | $a$ | $b/a$ | $c/a$ | $\Phi$ |
|---|---|---|---|---|---|
| spheres | 2 | $4.2538 \cdot 10^{-2}$ | 1.0 | 1.0 | 0.6449 |
| oblate ellipsoids | 2 | $4.9684 \cdot 10^{-2}$ | 1.0 | 0.7 | 0.7193 |
| prolate ellipsoids | 2 | $5.5868 \cdot 10^{-2}$ | 0.7 | 0.7 | 0.7158 |
| superballs | 5 | $3.8392 \cdot 10^{-2}$ | 1.0 | 1.0 | 0.7843 |

graphs are useful to describe transport processes that occur in particle systems [1]. We therefore analyze the particle graph, which is formed by connecting neighboring particles, in terms of transport-relevant characteristics like the coordination number (degree of connectivity), edge length and the geometric tortuosity (windedness of percolation paths). In general, significant differences are observed when analyzing the windedness of paths (i.e., geometric tortuosity) through the particle graphs indicating that geometric tortuosity is a useful tool for characterization of granular packings. The pore-phase is analyzed by both, a pore-phase graph, obtained by a skeletonization of the pore-phase [30], and by other characteristics from stochastic geometry describing further aspects of the morphology of the pore-phase (spherical contact distances and chord length). In addition, we analyze the system of particle midpoints by characteristics of stationary and isotropic point processes in order to investigate the degree of interaction between neighboring particles.

The paper is organized as follows. Section 2 introduces the granular packing algorithm. In Section 3, the system of particle midpoints is analyzed as well as the particle graph. Section 4 describes the analysis of the pore graph, with further characteristics relevant to the pore-phase being introduced. Conclusions are given in Section 5.

## 2 Granular Packing Algorithm

In our simulations, we represent the particles as superellipsoids defined by the equation

$$\left(\frac{x}{a}\right)^m + \left(\frac{y}{b}\right)^m + \left(\frac{z}{c}\right)^m = 1, \tag{1}$$

where we refer to $m$ as the shape parameter, and $a$, $b$ and $c$ are the semi-major axis lengths. For $m = 2$, we recover the general formula for an ellipsoid. While for $m > 2$ we obtain increasingly cubical shapes. In the packings considered in this paper, the grains have at least two equal axes. More precisely, we consider four different systems consisting of spheres, oblate ellipsoids, prolate ellipsoids and superballs. All systems contain 2000 particles arranged in a unit box having predefined aspect ratios $b/a$ and $c/a$. The three semi-major axis lengths $a$, $b$ and $c$ result from the packing algorithm, which is described later on. For more details, see Table 1. Examples of superellipsoids with different shape parameters and aspect ratios are shown in Figure 1. The corresponding granular packings are visualized in Figure 2.

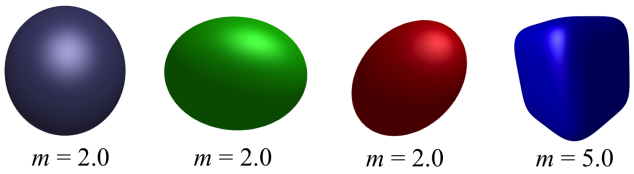


**Fig. 1** Images of the particle shapes (from left to right): sphere, oblate ellipsoid, prolate ellipsoid and superball.

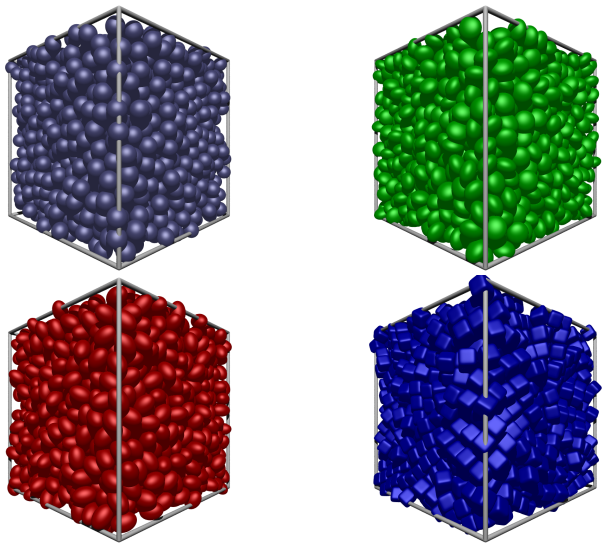

**Fig. 2** Visualizations of granular packings: spheres (top left), oblate ellipsoids (top right), prolate ellipsoids (bottom left) and superballs (bottom right).

Our packing algorithm utilizes a particle expansion technique to generate a dense jammed packing of superellipsoids. These types of techniques have been used extensively to study the properties of particle packings [7,12,24]. We seed our particles at random locations and with random orientations in a unit periodic box at a low packing fraction ($\Phi < 0.2$), where the particles all have unit density and are frictionless. We employ a fully dynamic linear spring Discrete-Element-Method (DEM) simulation to model the interaction between particles [6]. At each iteration we obtain the contact locations and linear overlaps between particles and hence solve for the forces and torques on each particle. (Further details of our DEM technique can be found in [4, 5].) The particles are then grown at a uniform volumetric growth rate $\gamma$ and a condition of constant kinetic energy is imposed on the system. The growth of the particles proceeds until a point is reached where the average overlap of the particles diverges sharply as the system jams. The growth rate affects the properties of the final packing and in the present paper was chosen such that random close packings of spheres and ellipsoids are formed [7].

## 3 Analysis of Particle Systems

### 3.1 Analysis of particle midpoints

In this section, we analyze the structural properties of the systems of particle midpoints. Thereby, we obtain quantitative information about the degree of spatial interaction between neighboring particle midpoints or particles midpoints with a certain distance, respectively. We use characteristics which are commonly applied in the analysis of stationary and isotropic point processes, see for example [21].

#### *3.1.1 Pair-correlation function*

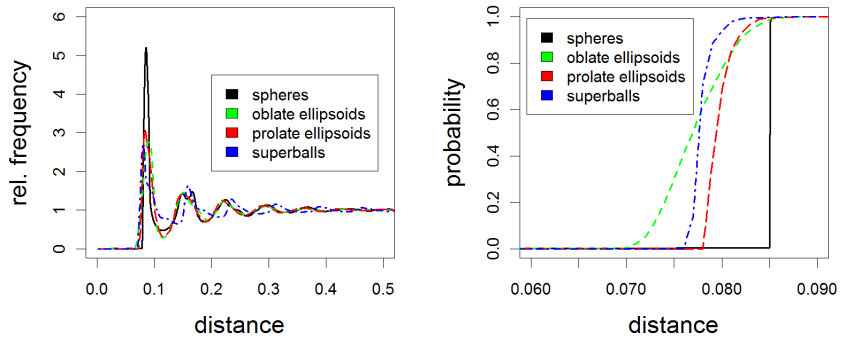


**Fig. 3** Pair-correlation function (left) and nearest-neighbor distance distribution function (right)

First we analyze the pair-correlation function $g : [0, \infty) \to [0, \infty)$, a second-order characteristic which has recently been considered in [3] to investigate random packings of ellipsoids. This characteristics measures the probability of finding a particle at a distance of $r$ away from a given reference particle, with the value $g(r)$ of the pair-correlation function being proportional to the relative frequency of point pairs with a distance of $r$. It is normalized such that in the case of complete spatial randomness (CSR, i.e., homogeneous Poisson process), we have $g(r) \equiv 1$. Furthermore, $g(r) > 1$ indicates a clustering of points and $g(r) = 1$ indicates no interaction of points, while $g(r) < 1$ indicates low probability to find pairs of points with distance $r$. In a 'regular' point process, i.e., a point process with both a high intensity of points and large distances between points, the pair-correlation function exhibits oscillations. Imagine points on a (slightly perturbed) regular lattice with width $d$. Then distances between points can only be close to the square roots of sums

of $(n_1 d)^2, (n_2 d)^2, (n_3 d)^2$ with $n_1, n_2, n_3 \geq 0$. Therefore, the pair-correlation function will only have peaks at these values.

For the particle packings, we see that the highest peak appears for the spheres, see Figure 3 (left). This is due to the constant distance from the surface of a sphere to its center, which leads to all its contacting grains having the same distance between grain centers and thus a high probability to find pairs of grains at this distance. The first peak for the other three shapes is lower and broader, due to the range of distances from the surface of the grains to their centers as a result of their non-spherical shape. All the grain shapes then exhibit decaying oscillations in the pair-correlation function for larger distances.

#### *3.1.2 Nearest-neighbor distance*

Next, we consider the distribution function of nearest-neighbor distances. From a so-called 'typical grain', we analyze the distribution of the distances from the center point to the center of its nearest-neighbor. Considering Figure 3 (right), we see that there are significant differences for the different grains shapes. The system of spheres has - as expected - a constant nearest-neighbor distance, corresponding to twice the sphere radius. There are large differences between the prolate and oblate ellipsoids, due to the differences in their semi-minor and semi-major axis lengths. For both ellipsoid cases the probability of a neighboring contact occurring becomes non-zero at twice the semi-minor axis length. The rate of increase in the probability for the prolate grains is much higher than for the oblate grains, this shows that there is reduced variation in the nearest-neighbor distances for the prolate grains due to two of their axes having the shorter relative length, compared to one for the oblate grains. For the system of superballs, the probability of a neighboring contact becomes non-zero at twice the distance from the center to a face on the grain's surface. The probability again increases at a fast rate, due to the prevalence for face on face contacts within the system, which leads to a low variability in the nearest-neighbor distances.

### 3.2 Analysis of particle graph

Spatial graphs are widely applied to analyze or simulate complex structures in biology, materials science and many other areas, see [1,25,30,32]. In particular, spatial graphs are useful to describe transport processes that occur in particle systems. Previous use of graph theory to study granular materials has focused on investigations of systems of spherical particles and has mainly considered the properties of the force network [19,33]. Here we will extend this consideration to a much more detailed consideration of the geometrical properties of both the solid phase and the pore-phase within systems of both spherical and non-spherical grains. A graph $G$ can be described by the pair $G = (V, E)$, see [11], where $V = \{\mathbf{x}_1, \ldots, \mathbf{x}_n\} \subset \mathbb{R}^3$ is a set of vertices and

$E = \{(\mathbf{x}_{i_1}, \mathbf{x}_{j_1}), \dots (\mathbf{x}_{i_k}, \mathbf{x}_{j_k}), \mathbf{x}_{i_l} \neq \mathbf{x}_{j_l} \in V\} \subset V \times V$ a set of edges. Graphs can describe the main structural aspects of the granular systems and therefore are a useful tool for the analysis and characterization of granular systems.

In order to apply spatial graphs to the granular systems, we transform the system of particles on a voxel grid with resolution $500 \times 500 \times 500$. This discretisation is especially useful for extraction of the pore-phase graph, see Section 4.2, since graph-extraction algorithms are available for voxel-based systems. Furthermore, the discretisation allows for a less complex approach to calculate distances between particles or distances of the pore-phase to the particle system more easily.

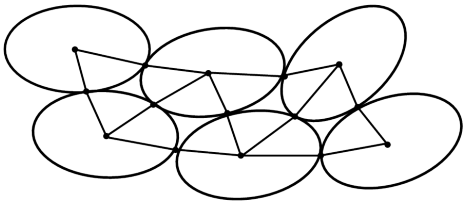

**Fig. 4** Illustration of particle graph

We now connect neighboring particles to form a graph, where we define two particles to be 'connected' if their smallest distance is below a threshold $\varsigma = 0.002$. This corresponds to two particles on the voxel grid having a common face. Two particles are connected from their midpoints via edges set at their 'touching point', i.e., at the point on the particle with the lowest distance to its connected neighbor, see Figures 4 and 5.

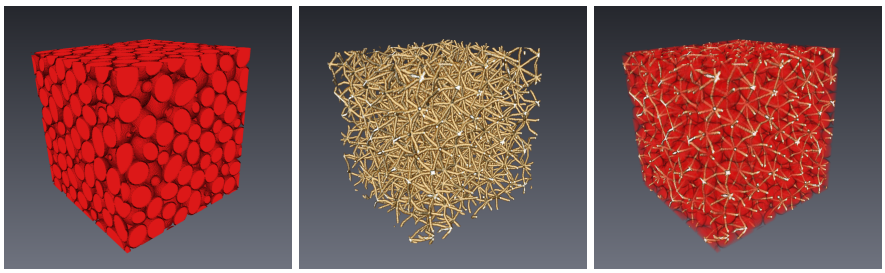

**Fig. 5** Left: particle system (prolate ellipsoids, cut-out); center: corresponding particle graph; right: particle system with particle graph

Such a particle graph can for example be used to describe charge transport (i.e., electron hopping) in a network of molecules, see [1,32], where the particles resemble molecules. Transport properties within the system of particles are related to the structure of the particle graph. Therefore, a structural characterization of this graph is important.

### *3.2.1 Graph coordination number*

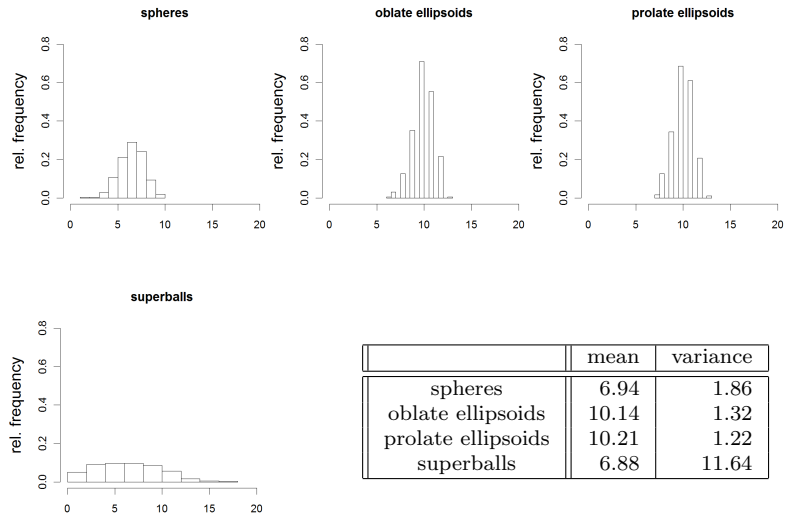


| | mean | variance |
|---|---|---|
| spheres | 6.94 | 1.86 |
| oblate ellipsoids | 10.14 | 1.32 |
| prolate ellipsoids | 10.21 | 1.22 |
| superballs | 6.88 | 11.64 |

**Fig. 6** Distributions of coordination numbers, together with their means and variances

To begin with, we consider the distribution of the coordination number of the graph, i.e., the number of edges emanating from a vertex. Large coordination numbers of the graph indicate a better connectivity. The results in Figure 6 show that the mean coordination number of the graph is as expected close to the mean number of contacts within the particle system [7]. The sphere graph has a mean coordination number of 6.94, while the ellipsoid cases both show an increase in coordination to 10.14 and 10.21, respectively. This is due to the additional number of grain contacts required for mechanical stability for a frictionless set of non-spherical particles. The superball graph has a lower mean coordination number than the ellipsoids, with a value of 6.88 being found. The lower value compared with the ellipsoid systems is due to the additional stability that face-on-face contacts provide in systems of non-spherical particles, which leads to a lower mean contact number. The shape of the distributions of coordination numbers for the sphere and ellipsoid systems are quite similar, being close to centered at the mean contact number and reasonably symmetric about the mean. Despite the higher mean coordination number, the variance in the contact number is lower for the ellipsoids than for the sphere system. For the superballs system, the distribution is much flatter with a very high variance of 11.64 being found.

### *3.2.2 Edge length*

Next, we analyze the distribution of edge lengths. In particle graphs that describe charge transport (i.e., electron hopping or hopping of holes), the distances between connected particles play an important role [1,32]. The mean value of the edge lengths is seen to correlate with the density of the overall packing within the unit cube, with superballs having the largest mean edge length, followed by the ellipsoids and then the spheres, see Figure 7. Furthermore, the mean values for both ellipsoid systems are identical, but the variance is larger for the prolate system. The variance for the superballs is smaller than for both ellipsoid systems. This may in part be due to the large number of face-on-face contacts in the superball system, which reduces the variability in the location of the contacts between neighboring grains.

Figure 7 (left) shows the cumulative distribution functions of the edge lengths of the graphs. For each grain shape the probability becomes non-zero for an edge of a given length to exist at the semi-minor axis length. For the sphere system, the edge lengths exhibit small variations described by the distance over which the probability varies from 0 to 1. This is due to two spheres being connected if their distance is within the interval $[0, \varsigma]$. The ellipsoids and superballs show smooth variations from their semi-minor to semi-major axis lengths (which is the distance from the particle center to its corner in the superball case). Comparing the curves for the prolate and oblate ellipsoids, we see that the prolate ellipsoids show a faster initial increase at distances above their the semi-minor axis length and then a slower increase at larger edge-lengths, compared to the oblate ellipsoids which have an initial slower increase for the shorter edge-lengths and then a more rapid increase at larger edge lengths. These differences are attributable to how the total surface area of the ellipsoids varies with the distance from the center of the grain. For the prolate ellipsoids with 2 shorter axes, there is a relatively larger proportion of the total surface area at shorter distances from the center of the ellipsoid, compared to the oblate ellipsoid which has 2 longer axes.

### *3.2.3 Geometric tortuosity*

We consider the geometric tortuosity to describe the windedness of percolation pathways along the particle graph in a similar manner to that described in [32]. Assume that point particles (modelling e.g. charge carriers) move from the top of the granular system to the bottom, where the paths are restricted to edges of the graph. Then, for a given vertex $\mathbf{x}_i = (x_i, y_i, z_i) \in \mathbb{R}^3$, located at the top of the granular system, we are interested in the shortest path (along the edges of the graph) towards a vertex located at the bottom of the system, say, $\mathbf{x}_j$. If $\overrightarrow{\mathbf{x}_i\mathbf{x}_j}$ is the shortest path between vertices $\mathbf{x}_i$ and $\mathbf{x}_j$ and $d_z(\mathbf{x}_i, \mathbf{x}_j)$ denotes their orthogonal distance $|z_i - z_j|$ in $z$-direction, then the geometric tortuosity $\tau(\mathbf{x}_i, \mathbf{x}_j)$ is defined as $\frac{|\overrightarrow{\mathbf{x}_i\mathbf{x}_j}|}{d_z(\mathbf{x}_i,\mathbf{x}_j)}$, thus the ratio between the length $|\overrightarrow{\mathbf{x}_i\mathbf{x}_j}|$ of the path $\overrightarrow{\mathbf{x}_i\mathbf{x}_j}$ along the graph and the orthogonal distance $d_z(\mathbf{x}_i, \mathbf{x}_j)$ between

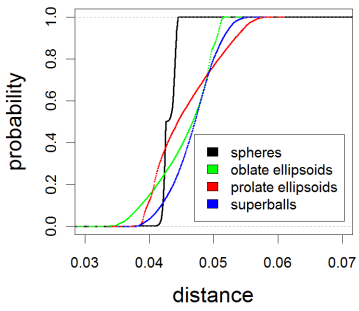


| | mean | variance |
|---|---|---|
| spheres | $4.31 \cdot 10^{-2}$ | $7.69 \cdot 10^{-7}$ |
| oblate ellipsoids | $4.55 \cdot 10^{-2}$ | $1.92 \cdot 10^{-5}$ |
| prolate ellipsoids | $4.55 \cdot 10^{-2}$ | $2.57 \cdot 10^{-5}$ |
| superballs | $4.68 \cdot 10^{-2}$ | $1.24 \cdot 10^{-5}$ |

**Fig. 7** Left: cumulative distribution functions of edge lengths; right: their means and variances

both vertices $\mathbf{x}_i$ and $\mathbf{x}_j$. Different vertices as starting points will yield different values of geometric tortuosity, wherefore we are interested in the distribution of geometric tortuosity.

Geometric tortuosity is a structural parameter characterizing morphologies and is typically related to the porosity which is one minus packing fraction. If a structure has a porosity of zero, the geometric tortuosity of the solid phase will be one, whereas a porosity close to one will, in general, yield very large values of geometric tortuosity of the solid phase. Often, values of geometric tortuosity lie between 1 and 2, see [15,16,31]. Besides porosity and a constrictivity factor ('bottleneck' criterion), (geometric) tortuosity is considered an important (morphological) characteristic that influences effective transport properties. In particular, effective conductivity is described as being inversely proportional to tortuosity, where the notion of tortuosity may not necessarily refer to geometric tortuosity, as various definitions of tortuosity exist (e.g. hydraulic tortuosity, dielectrical tortuosity, diffusional tortuosity), see [20].

Given the above definition of geometric tortuosity, smaller values of tortuosity indicate less winded paths which (generally) leads to faster transport while higher values, thus more winded paths, lead to slower transport.

To estimate the geometric tortuosity distribution of the particle graphs, we calculate the shortest path lengths from vertices on the top to the bottom (and vice versa). Therefore, we cut off all vertices within a certain layer on the top and within a certain layer on the bottom. For each vertex at the top (bottom), we calculate the shortest distance to the closest point at the bottom (top) and use this value to estimate the geometric tortuosity. To increase the accuracy of the estimation (i.e., increase the number of data points), we consider geometric tortuosities not only in $z$-direction, but also in $x$- and $y$-directions (and adjusting $d_z(\mathbf{x}_i, \mathbf{x}_j)$ to $d_x(\mathbf{x}_i, \mathbf{x}_j)$ and $d_y(\mathbf{x}_i, \mathbf{x}_j)$, resp.). Since the granular systems are isotropic, the distribution of geometric tortuosity is the same for all directions considered.

The results for the computations of the geometric tortuosity of the granular packings are shown in Figure 8. The two systems of ellipsoids have the lowest tortuosity characteristics, both in terms of the lowest mean values and the lowest variances. The sphere system has a higher mean and a larger variance. This is interesting as it appears to suggest that introducing anisotropy into the shape of a grain by transitioning from a spherical to an elliptical grain can improve the transport properties within the granular system. Several factors in the structural differences between sphere and ellipsoid packings lead to this decrease in tortuosity. There is an increase in density for ellipsoids compared to spheres (Table 1), with the system still maintaining a high degree of disorder. The higher mean coordination number of the ellipsoid systems also reduces tortuosity, as there is an increase in the number of available pathways from each grain to its neighbors. This increase in the number of connections, increases the likelihood of finding a connection that is closer to the straight path between the start and end points. Interestingly, the two ellipsoid systems are almost indistinguishable, while differing significantly from the other granular packings.

The superballs are both the most ordered and the densest system, however we see that this does not necessarily mean that the granular network will exhibit better transport properties, with the superball packings having the highest mean tortuosity and the highest variance. This suggests an inhibition of transport in any process that must proceed through the system traveling from particle to particle. Given the high density and relatively low coordination number compared to the ellipsoid system, this suggests that the coordination number is the biggest influence on tortuosity. It should be noted however that here we are considering the network of particle centers and thus this measure is relevant to transport properties that are required to pass through the center of the particles. Transport through the system that could proceed via the shortest line through the solid phase, could take a less winded path due to not needing to travel through the center of each grain.

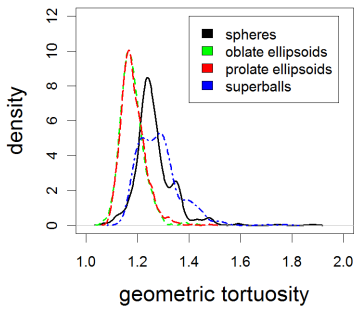


| | mean | variance |
|---|---|---|
| spheres | 1.26 | $5.72 \cdot 10^{-3}$ |
| oblate ellipsoids | 1.18 | $2.10 \cdot 10^{-3}$ |
| prolate ellipsoids | 1.18 | $2.27 \cdot 10^{-3}$ |
| superballs | 1.28 | $6.42 \cdot 10^{-3}$ |

**Fig. 8** Left: distributions of geometric tortuosity; right: their means and variances

## 4 Analysis of Pore-Phase

In this section, we analyze the pore-phase, which is the space complementary to the union of particles. In various applications of granular systems, objects (e.g. fluids or gases) are transported in the pore-phase. It is thus important to characterize morphological aspects of the pore-phase and consider their relation to associated transport properties.

### 4.1 Analysis of characteristics of spatial extent

#### *4.1.1 Chord length*

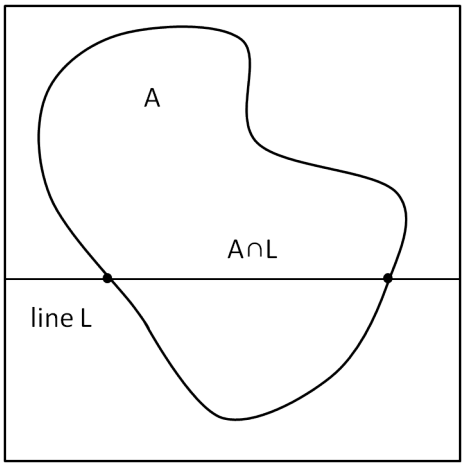


**Fig. 9** Line $L$ intersecting an object $A$

We first consider the distribution of chord lengths [27]. In general, the chord length with respect to a line $L$ for an object $A \subset \mathbb{R}^3$ is the length of the intersecting line segment $L \cap A$ (Figure 9). In the case of a non-convex shape of the object $A$, each intersecting line segment is considered as a separate chord. Considering all lines with a fixed direction $u \in \partial B(o,1)$, with $\partial B(o,1)$ being the unit sphere, yields the chord length distribution (for this direction). Thus, the chord length distribution is the distribution of the extent of an object $A$ in direction $u$. Here, we consider chord lengths of the pore-phase, i.e., $A$ represents the pore-phase, averaged over $x-, y-$ and $z-$ direction. The results in Figure 10 (right) show that the pore-phase is largest in terms of its mean spatial extent for the sphere system, followed by the two ellipsoids. The pore-phase of the system of superballs exhibits a smaller mean chord-length. The mean chord length inversely correlates with the density of the packings, ordering from spheres, to ellipsoids, to superballs. The longer mean chord length

suggests a tendency for better transport properties, with on average greater distances within the pore space existing over which transport can proceed uninteruptted by the solid phase.

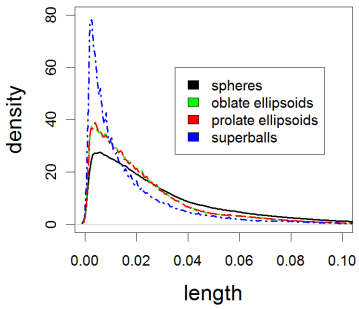


| | mean | variance |
|---|---|---|
| spheres | 0.031 | $8.51 \cdot 10^{-4}$ |
| oblate ellipsoids | 0.023 | $4.76 \cdot 10^{-4}$ |
| prolate ellipsoids | 0.023 | $4.84 \cdot 10^{-4}$ |
| superballs | 0.018 | $4.21 \cdot 10^{-4}$ |

**Fig. 10** Left: distributions of chord lengths; right: their means and variances.

### *4.1.2 Spherical contact distance*

Next, we analyze the spherical contact distribution function $H : [0, \infty) \to [0, 1]$ of the pore-phase, where the value $H(r)$ denotes the probability to reach a particle from a randomly chosen point of the pore-phase within a distance smaller or equal than $r$ [27]. The results in Figure 11 show that the pore-phase of the isotropic sphere system has by far the largest mean spherical contact distance, which suggests the largest spatial extent of the pore-phase.

Among the cumulative distribution functions shown in Figure 11, the sphere curve is consistently underneath that of the other 3 packings, indicating that the sphere system has the most compact pore space, i.e., for a randomly chosen location of the pore-phase, the chance that a sphere with any given radius could be placed within the pore space is largest for the pore space of the sphere packing. The superballs curve is above the 2 ellipsoid curves for smaller distances, indicating that the pore-phases of the ellipsoid systems possess less narrow pore sections compared to the superball system. The superball and the ellipsoid curves intersect at a distance of approximately 0.01, after which the ellipsoid curves lie just above the superballs curve. This indicates that the superballs have a greater fraction of pores that can contain larger spheres. These curves give us useful information on the relative sizes and shapes of the pores in the different packings, which can be useful in indicating how transportation, in particular of particles of different sizes, will proceed through the packing.

The results agree with the trend observed for chord lengths, see Section 4.1.1. The differences, especially for the prolate and oblate ellipsoids appear minor. Note that the spherical contact distance distribution, however, averages over the whole pore-phase. In Section 4.2.4, we will consider another

pore-phase characteristic of this type, where we analyze the spherical contact distances evaluated from points on the pore-phase graph.

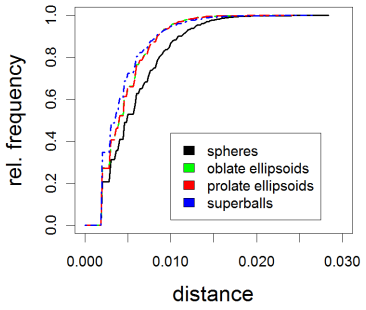


| | mean | variance |
|---|---|---|
| spheres | $5.93 \cdot 10^{-3}$ | $1.42 \cdot 10^{-5}$ |
| oblate ellipsoids | $4.69 \cdot 10^{-3}$ | $7.71 \cdot 10^{-6}$ |
| prolate ellipsoids | $4.67 \cdot 10^{-3}$ | $7.63 \cdot 10^{-6}$ |
| superballs | $4.39 \cdot 10^{-3}$ | $8.99 \cdot 10^{-6}$ |

**Fig. 11** Left: cumulative distribution functions of spherical contact distances; right: their means and variances

## 4.2 Analysis of pore-phase graph

In many systems, like the gas-diffusion layer in PEM fuel cells, the 3D morphology of the pore-phase plays an important role and thus, an analysis of the pore-phase by analyzing *individual pores* appears reasonable. There is however an inherent difficulty in defining what constitutes an individual pore in a granular structure and no universally accepted definition or algorithm exists. Techniques include the use of watershed algorithms [17], or graph-based techniques [30]. The watershed technique, in its classical version, suffers from over-segmentation and given the complex geometry of the pore-phase of the granular systems, the watershed technique appears inadequate. Graph-based techniques aim to describe the pore-phase by a graph, where the nodes are interpreted as centers of the pores and edges describe connections between neighboring pore centers which are separated by pore-throats (i.e., pore bottlenecks). As described above, the geometry of the pore-phase is rather complex and thus, a pore-phase graph may not match with this interpretation (i.e., considering vertices are pore centers).

Thus, we shift our focus in the analysis away from investigating individual pores towards investigating the pore-phase as a whole. For this purpose, the graph-based technique is adequate. More precisely, to analyze the pore-phase, we extract the pore-phase graph by a skeletonization process using the commercial software Avizo with its default settings [14,34].

In general, if a morphology consists of a solid phase and a pore-phase, then the idea of the skeletonization for the pore-phase is to change pore-phase voxels into solid voxels such that a thin line with thickness one of pore-phase voxels remains, see Figure 12 (a). Furthermore, the skeletonization is homotopic,

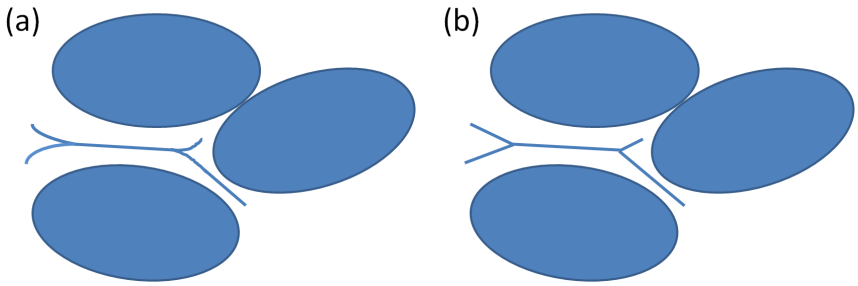


**Fig. 12** Cartoon of pore-phase skeletonization (a) and approximation by graph (b)

i.e., connectivity-preserving. In the next step, the skeleton is transformed into vector data, i.e., it is approximated by polygonal tracks, see Figure 12 (b). These polygonal tracks are systems of line segments. The representation by systems of line segments can be interpreted as a spatial graph, where the start- and endpoints of the line segments form the set of vertices and the line segments themselves the set of edges.

Note that we do not interpret the vertices of the graph as pore centers, but we use characteristics of the graph to obtain valuable information with respect to differences in the pore-phases for the different granular packings considered in this paper.

**Fig. 13** Left: particle system (prolate ellipsoids, cut-out); center: corresponding pore-phase graph; right: particle system with pore-phase graph

### *4.2.1 Coordination number*

The distribution of the coordination number of the nodes of the pore-phase graph, as displayed in Figure 14, is quite similar for all four superellipsoids considered in the present paper. The two ellipsoid systems have virtually identical means and variances. The sphere system has a slightly lower mean value and a slightly higher variance compared to the ellipsoid systems. This indicates that transitioning from a spherical to an ellipsoidal system of particles increases the overall connectivity of the pore space. However, this increase is more subtle

compared to the large increase in coordination number for the solid phase in going from spheres to ellipsoids. The coordination number of the superball system lies between that of the spheres and the ellipsoids.

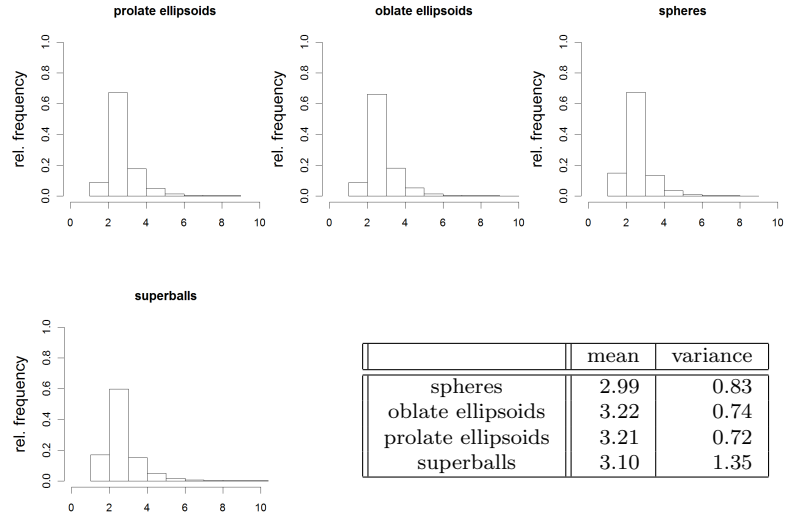


| | mean | variance |
|---|---|---|
| spheres | 2.99 | 0.83 |
| oblate ellipsoids | 3.22 | 0.74 |
| prolate ellipsoids | 3.21 | 0.72 |
| superballs | 3.10 | 1.35 |

**Fig. 14** Distributions of coordination numbers, together with their means and variances

### *4.2.2 Edge length*

The distribution of edge lengths of the pore-phase graph is shown in Figure 15. The mean edge length and the variance decrease as the density of the packings increases going from spheres, to ellipsoids, to superballs. The shapes of the edge length distributions are quite similar for the different packings. In particular, we again observe that the two different ellipsoid packings have virtually identical edge length distributions.

### *4.2.3 Geometric tortuosity*

All computed values of geometric tortuosity of the pore-phase are between 1.35 and 1.39, see Figure 16. Interestingly, these values are within the range of geometric tortuosity recently found in an analysis of the pore-phase of LSC cathodes made from sintered (spherical) particles, where values between 1.21 and 1.41 were found [16]. This is relatively low compared to the geometric tortuosity found in a study of the pore-phase of a gas diffusion layer made from disordered strongly curved fibers, where a mean value of geometric tortuosity of 1.6 was obtained [15].

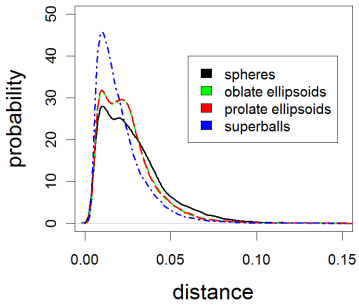


| | mean | variance |
|---|---|---|
| spheres | $2.78 \cdot 10^{-2}$ | $3.27 \cdot 10^{-4}$ |
| oblate ellipsoids | $2.46 \cdot 10^{-2}$ | $2.32 \cdot 10^{-4}$ |
| prolate ellipsoids | $2.46 \cdot 10^{-2}$ | $2.37 \cdot 10^{-4}$ |
| superballs | $2.06 \cdot 10^{-2}$ | $1.89 \cdot 10^{-4}$ |

**Fig. 15** Left: distributions of edge lengths; right: their means and variances

Analyzing the distribution of geometric tortuosity, we see a strong similarity across the different packings considered, see Figure 16. This is particularly interesting since the geometric tortuosities exhibited major differences when analyzing the particle graph, see Section 3.2.3. The systems with more anisotropic grains shapes (ellipsoids and superballs) have a smaller mean geometric tortuosity, while in the sphere system, geometric tortuosity is larger.

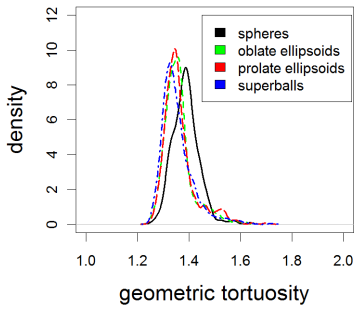


| | mean | variance |
|---|---|---|
| spheres | 1.39 | $2.60 \cdot 10^{-3}$ |
| oblate ellipsoids | 1.36 | $3.32 \cdot 10^{-3}$ |
| prolate ellipsoids | 1.36 | $4.02 \cdot 10^{-3}$ |
| superballs | 1.35 | $3.80 \cdot 10^{-3}$ |

**Fig. 16** Left: distributions of geometric tortuosity; right: their means and variances

The mean geometric tortuosity is smallest for the superballs, which could suggest good transport properties. But a shortest path may not always represent the fastest or the best route to travel. Consider analogously a situation in the real world where one wishes to find the best driving route to travel from $A$ to $B$. This is a tradeoff between shortest paths (which might involve narrow minor roads) and large highways (which might include detours). In Section 4.1 we showed that the superball system has the smallest extent of pore-phase. Thus, to decide which of the considered granular packings has the best transport properties of the pore-phase, will depend on the specific physical application. When for example considering the liquid flow, computational

fluid dynamics has been demonstrated to be a useful tool in determining the permeability in granular systems similar to those considered here [28].

### *4.2.4 Graph-based spherical contact distance*

In Section 4.1, we have seen that the structural differences between the pore-phases of oblate and prolate ellipsoids were insignificant with respect to the characteristics considered in that section. We therefore assume, together with the other characterization results of the pore-phase obtained so far in Section 4.2, that the pore-phases are indeed very similar for prolate and oblate ellipsoids. We now consider again the spherical contact distances, but only evaluated from points on the graph. If differences regarding spherical contact distances exist, they should be more significant when analyzing the pore-phase from the graph which is located predominantly in the center of the pores. Thus, the distribution of these graph-based spherical contact distances gives accurate information of the sizes of the pores. The results in Figure 17 show the pore-phase is most narrow for the superball system and again, that the spatial extent is largest for the sphere system. Again, the differences between the prolate and oblate ellipsoid system are very small.

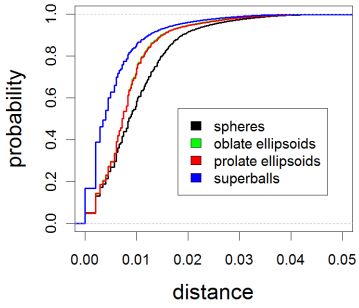


| | mean | variance |
|---|---|---|
| spheres | $10.06 \cdot 10^{-3}$ | $5.51 \cdot 10^{-5}$ |
| oblate ellipsoids | $8.30 \cdot 10^{-3}$ | $3.85 \cdot 10^{-5}$ |
| prolate ellipsoids | $8.38 \cdot 10^{-3}$ | $4.02 \cdot 10^{-5}$ |
| superballs | $5.48 \cdot 10^{-3}$ | $3.69 \cdot 10^{-5}$ |

**Fig. 17** Left: cumulative distribution functions of spherical contact distances evaluated on the nodes of the pore-phase graph; right: their means and variances

## 5 Conclusions

In this paper, we considered a set of computationally generated granular packings and performed an extensive series of analyses to quantify the geometric properties of both the solid and the pore-phase. A particle graph was generated by connecting neighboring particles and analyzed in terms of transport-relevant characteristics like the degree of connectivity (coordination number), edge lengths and the windedness of percolation paths (geometric tortuosity). Similarly, the pore-phase was analyzed by a pore-phase graph, obtained by

a skeletonization of the pore-phase, as well as by further characteristics from stochastic geometry describing the spatial extent of the pore-phase (spherical contact distances and chord lengths).

In terms of transport properties, the pore-phase of the superball system has the least winded percolation paths (i.e., the smallest geometric tortuosity), yet it also has the smallest mean chord length indicating the smallest pore-phase in terms of their spatial extent. Contrarily, the pore-phase of the sphere system has the most winded paths (i.e., the largest geometric tortuosity), but the largest mean chord length. Goodness of transport properties will be a tradeoff between large pores and short paths, and will depend on the specific physical application. Overall, the characterization of the pore-phases of the four granular packings considered in this paper exhibited a surprisingly large degree of similarity. Moreover, the shape of the distributions characterizing the pore-phases, were all of the same shape indicating a similar morphological structure of the pore-phase. In particular, the pore-phase for the 2 ellipsoid packings (oblate and prolate) show a striking degree of similarity for all the measures considered here.

## References


1. Baumeier, B., Stenzel, O., Poelking, C., Andrienko, D. and Schmidt, V. (2012). Stochastic Modeling of Molecular Charge Transport Networks. *Physical Review B*, **86**, 184202.
2. Bernal, J. D. and Mason, J. (1960). Packing of Spheres: Co-ordination of Randomly Packed Spheres. *Nature*, **188**, 910–911.
3. Bezrukov, A. and Stoyan, D. (2006). Simulation and Statistical Analysis of Random Packings of Ellipsoids. *Particle & Particle Systems Characterization*, **23**, 388–398.
4. Cleary, P. W. (1998). Predicting Charge Motion, Power Draw, Segregation and Wear in Ball Mills Using Discrete Element Methods. *Minerals Engineering*, **11**, 1061–1080.
5. Cleary, P. W. (2008). The Effect of Particle Shape on Simple Shear Flows. *Powder Technology*, **179**, 144–163.
6. Cundall, P. and Strack, O. (1979). A Discrete Numerical Model for Granular Assemblies. *Geotechnique*, **29**, 47–65.
7. Delaney, G. W. and Cleary, P. W. (2010). The Packing Properties of Superellipsoids. *EPL (Europhysics Letters)*, **89**, 34002.
8. Delaney, G. W., Hilton, J. E. and Cleary, P. W. (2011). Defining Random Loose Packing for Non-spherical Grains. *Physical Review E*, **83**, 051305.
9. Delaney, G. W., Matteo, T. D. and Aste, T. (2010). Combining Tomographic Imaging and DEM Simulations to Investigate the Structure of Experimental Sphere Packings. *Soft Matter*, **6**, 2992–3006.
10. Delaney, G. W., Weaire, D., Hutzler. S. and Murphy, S (2005). Random Packing of Elliptical Disks. *Philosophical Magazine Letters*, **85**, 89–96.
11. Diestel, R. (2005). *Graph Theory.* Heidelberg: Springer.
12. Donev, A., Cisse, I., Sachs, D., Variano, E. A., Stillinger, F. H., Connelly, R., Torquato, S. and Chaikin, P. M. (2004). Improving the Density of Jammed Disordered Packings Using Ellipsoids. *Science*, **303**, 990–993.
13. Farr R.S. and Groot R.D. (2009). Close packing density of polydisperse hard spheres *J. Chem. Phys.*, **131**, 244104.
14. Fourard, C., Malandain G., Prohaska, S. and Westerhoff, M. (2006). Blockwise Processing Applied to Brain Microvascular Network Study. *IEEE Trans. Med. Im.*, **25**, 1319–1328
15. Gaiselmann, G., Thiedmann, R., Manke, I., Lehnert, W. and Schmidt, V. (2012). Stochastic 3D modeling of fiber-based materials. *Computational Materials Science*, **59**, 75–86.

16. Gaiselmann, G., Neumann, M., Holzer, L., Hocker, T., Prestat, M. and Schmidt, V. (2013). Stochastic 3D modeling of LSC cathodes based on structural segmentation of FIB-SEM images. *Computational Materials Science*, **67**, 48–62.
17. Godehardt, M. and Schladitz, K. (2006). Geometric Characterisation of Light Weight Composites Using Computer Tomographic Images. Proceedings of the 9th European Conference of Non-Destructive Testing, Berlin, 25.-29. September 2006.
18. Hales, T. (2005). A Proof of the Kepler Conjecture. *Annals of Mathematics*, **162**, 1065–1185.
19. Hilton, J. E., Cleary, P. W. and Tordesillas, A. (2013). Unitary Stick-slip Motion in Granular Beds. *AIP Conference Proceedings*, **1542**, 843-846.
20. Holzer, L. and Wiedenmann, D. and Münch, B. and Keller, L. and Prestat, M. and Gasser, Ph. and Robertson, I. and Grobéty, B. (2013). The influence of constrictivity on the effective transport properties of porous layers in electrolysis and fuel cells. *Journal of Materials Science*, **48**, 2934–2952.
21. Illian, J., Penttinen, A., Stoyan, H. and Stoyan, D. (2008). *Statistical Analysis and Modelling of Spatial Point Patterns*. Chichester: J. Wiley & Sons.
22. Jaeger, H. M., Nagel, S. R. and Behringer, R. P. (1996). Granular Solids, Liquids, and Gases. *Review of Modern Physics*, **68**, 1259–1273.
23. Kadanoff, L. P. (1999). Built Upon Sand: Theoretical Ideas Inspired by the Flow of Granular Materials. *Review of Modern Physics*, **71**, 435–444.
24. Lubachevsky, B. D. and Stillinger, F. H. (1990). Geometric Properties of Random Disk Packings. *Journal of Statistical Physics*, **60**, 561–583.
25. Lueck, S., Sailer, M., Schmidt, V. and Walther, W. (2010). Three-dimensional Analysis of the Intermediate Filament Network Using SEM-Tomography. *Journal of Microscopy*, **239**, 1–16.
26. Münch, B. and Holzer, L. (2008). Contradicting Geometrical Concepts in Pore Size Analysis Attained with Electron Microscopy and Mercury Intrusion. *Journal of the American Ceramic Society*, **91**, 4059–4067.
27. Ohser, J. and Mücklich, F. (2000). *Statistical Analysis of Microstructures in Materials Science*. Chichester: J. Wiley & Sons.
28. Pereira, G. G., Dupuy, P. M., Cleary, P. W. and Delaney, G. W. (2012). Comparison of Permeability of Model Porous Media between SPH and LB. *Progress in Computational Fluid Dynamics*, **12**, 176–186.
29. Williams S.R. and Philipse A.P. (2003). Random packings of spheres and spherocylinders simulated by mechanical contraction. Physical Review E, **67**, 051301.
30. Thiedmann, R., Hartnig, C., Manke, I., Schmidt, V. and Lehnert, W. (2009). Local Structural Characteristics of Pore Space in GDL's of PEM Fuel Cells based on Geometric 3D Graphs. *Journal of the Electrochemical Society*, **156**, B1339–B1347.
31. Thiedmann, R., Stenzel, O., Spettl, A., Shearing, P. R., Harris, S. J., Brandon, N. P. and Schmidt, V. (2011). Stochastic simulation model for the 3D morphology of composite materials in Li-ion batteries. *Computational Materials Science*, **50**, 3365–3376.
32. Thiedmann, R., Spettl, A., Stenzel, O., Zeibig, T., Hindson, J. C., Saghi, Z., Greenham, N. C., Midgley, P. A. and Schmidt, V. (2012). Networks of Nanoparticles in Organic-Inorganic Composites: Algorithmic Extraction and Statistical Analysis. *Image Analysis and Stereology*, **31**, 23–42.
33. Tordesillas, A. (2011). When Failure is an Option: Rewiring Granular Networks. *Multiscale and Multiphysics Processes in Geomechanics*, 33–36.
34. VSG – Visualization Sciences Group – Avizo Standard, Version 6.3, `http://www.vsg3d.com/avizo/standard`.
35. Athanassiadis A. G., Miskin M. Z., Kaplan P., Rodenberg N., Lee S.H., Merritt J., Brown E., Amend J., Lipson H. and Jaeger H.M. (2013). Particle Shape Effects on the Stress Response of Granular Packings. arXiv:1308.2241.
36. Neudecker, M., Ulrich S., Herminghaus S., and SchrÃ¶ter M (2013). Jammed Frictional Tetrahedra Are Hyperstatic. *Physical Review Letters*, 111 : 028001.
37. Damasceno, P.F., Engel M., and Glotzer S.C. (2012). Predictive Self-Assembly of Polyhedra into Complex Structures. *Science* 337, 6093 : 453-457.
38. Baram, R.M. and Lind, P.G. (2012). Deposition of general ellipsoidal particles. *Phys. Rev. E* 85, 4 : 041301.

39. Liu, A. J. and Nagel, S.R. (1998). Nonlinear dynamics: Jamming is not just cool any more, *Nature* 396, 6706 : 21-22.
40. Aste T. and Weaire D. (2000). The Pursuit of Perfect Packing, Bristol and Philadelphia: IOP Publishing Ltd.